Nano Research 2015, 8(12): 3963–3971
DOI 10.1007/s12274-015-0899-3
Research Article
ISSN 1998-0124
CN 11-5974/O4

Arginine-mediated synthesis of cube-like platinum nanoassemblies as efficient electrocatalysts

Gengtao Fu[1], Qian Zhang[1], Jiayan Wu[1], Dongmei Sun[1], Lin Xu[1], Yawen Tang[1] (✉), and Yu Chen[2] (✉)

[1] *Jiangsu Key Laboratory of New Power Batteries, Jiangsu Collaborative Innovation Centre of Biomedical Functional Materials, School of Chemistry and Materials Science, Nanjing Normal University, Nanjing 210023, China*
[2] *Key Laboratory of Macromolecular Science of Shaanxi Province, School of Materials Science and Engineering, Shaanxi Normal University, Xi'an 710062, China*

Received: 7 August 2015
Revised: 6 September 2015
Accepted: 8 September 2015

KEYWORDS
platinum nanocrystals,
cube,
self-assembly,
arginine,
electrocatalysis

ABSTRACT

Controllable self-assembly of noble metal nanocrystals is of broad interest for the development of highly active electrocatalysts. Here we report an efficient arginine-mediated hydrothermal approach for the high-yield synthesis of cube-like Pt nanoassemblies (Pt-CNAs) with porous cavities and rough surfaces based on the self-assembly of zero dimensional Pt nanocrystals. In this process, arginine acts as the reductant, structure directing agent, and linker between adjacent nanocrystals. Interestingly, the Pt-CNAs exhibit single-crystal structures with dominant {100} facets, as evidenced by X-ray diffraction. Based on electrocatalytic studies, the as-synthesized Pt-CNAs exhibit improved electrocatalytic activity as well as good stability and CO tolerance in the methanol oxidation reaction. The Pt-CNA's good performance is attributed to their unique morphology and surface structure. We believe that the synthetic strategy outlined here could be extended to other rationally designed monometallic or bimetallic nanoassemblies for use in high performance fuel cells.

1 Introduction

Well-defined nanoassemblies consisting of small nanocrystals have received considerable attention due to their many unique structural characteristics, such as high porosity, large surface area per unit volume, interconnected open-pore structures, and stable frameworks [1–14]. To date, various strategies have been developed to fabricate nanoassemblies, such as surface modification [9], induced magnetic dipoles [10], electrostatic ordering [11], gravitational sedimentation [12], interface induction [13], and additional metal or ions [14]. For example, novel AuAg nanosheets were successfully prepared from AuAg nanowires by addition of Pluronic P123 surfactant and fusion of the AuAg nanowires [9]. Polycrystalline spherical Pt nanoassemblies could be obtained by self-assembly of Pt nanocubes in the presence of Fe^{3+} ions [14]. Although much effort has been devoted to the self-assembly of nanocrystals into

Address correspondence to Yawen Tang, tangyawen@njnu.edu.cn; Yu Chen, ndchenyu@gmail.com

various nanoassemblies, the controlled synthesis of such nanoassemblies with well-defined morphologies and single-crystal structures remains a challenge.

Amino acids, as the fundamental building blocks of proteins, have been widely employed in the synthesis of noble metal nanocrystals owing to their selective coordination of noble metal ions [15–20]. In particular, arginine is the only amino acid with a guanidino group consisting of four proton donor moieties (Scheme 1), and it easily interacts with carboxyl groups through strong hydrogen-bonding and electrostatic interactions [21, 22]. In addition, the strong coordination interaction between guanidino groups and noble metal ions efficiently slows the reduction of noble metal ions [23], which allows the synthesis to be kinetically controlled. Thus, due to its unique inherent properties, we rationally expect that noble metal nanoassemblies can be easily obtained using arginine molecules.

Following this line of inquiry, we report an effective, arginine-mediated self-assembly process for the synthesis of single-crystal cube-like Pt nanoassemblies (Pt-CNAs) with rough surfaces and dominant {100} facets in the presence of polyvinyl pyrrolidone (PVP). By varying the amount of arginine added, nanostructures with different degrees of self-assembly can be achieved. Relative to the commercial polycrystalline Pt black catalysts, Pt-CNAs possess a large proportion of exposed {100} facets with abundant active sites at the cubes' edges and corners; this morphology results in improved electrocatalytic activity, stability, and high CO tolerance in the methanol oxidation reaction (MOR).

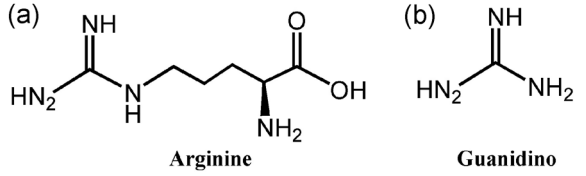

Scheme 1 Molecular structures of (a) arginine and (b) the guanidino group.

2 Experimental

2.1 Reagents and chemicals

Arginine was purchased from Shanghai Kayon Biological Technology CO., Ltd. (Shanghai, China). PVP (M_W = 30,000) and chloroplatinic acid hexahydrate ($H_2PtCl_6{\cdot}6H_2O$) were purchased from Sinopharm Chemical Reagent Co., Ltd (Shanghai, China). Commercial Pt black was purchased from Johnson Matthey Corporation. All reagents were of analytical reagent grade and used without further purification.

2.2 Synthesis of Pt-CNAs

In a typical synthesis, arginine (75 mg), PVP (400 mg), and 1 mL of H_2PtCl_6 solution (40 mM) were added into 9.0 mL of deionized water with continuous stirring for 10 min at room temperature. The homogeneous solution was transferred to a 20 mL Teflon-lined stainless steel autoclave and heated at 200 ˚C for 4 h. After being cooled to room temperature, the Pt-CNAs were separated by centrifugation at 20,000 rpm for 10 min, washed three times with ethanol, and then dried at 60 ˚C for 5 h in a vacuum oven. Finally, the Pt-CNAs were treated with UV irradiation at 185 and 254 nm in air for 4 h to remove the capping agent prior to electrochemical testing [24, 25].

2.3 Electrochemical measurements

All electrochemical experiments were performed using a CHI 660 C electrochemical analyzer (CH Instruments, Shanghai, Chenhua Co.). A standard three-electrode system was used for all electrochemical experiments, which consisted of a Pt wire as the auxiliary electrode, a saturated calomel electrode (SCE) as the reference electrode, and a catalyst-modified glassy carbon electrode as the working electrode. All potentials in this study were reported with respect to the SCE. All electrochemical measurements were carried out at 30 ˚C.

An evenly distributed suspension of catalyst was prepared by ultrasonic mixing of 10 mg catalyst and 5 mL H_2O for 30 min; 6 μL of the resulting suspension was drop-cast onto the surface of the glassy carbon electrode (3 mm diameter). After drying at room temperature, 3 μL of Nafion solution (5 wt.%) was drop-cast on the modified electrode surface and allowed to dry again. Thus, the working electrode was obtained. The specific loading of metal on the electrode surface was about 170 $\mu g{\cdot}cm^{-2}$. Electrochemical measurements were conducted in an N_2-saturated 0.5 M H_2SO_4 solution or an N_2-saturated 0.5 M H_2SO_4 solution

with 0.5 M CH_3OH. Prior to the electrochemical tests, the catalyst-coated electrodes were pre-treated by cycling the potential between –0.2 and 1.2 V vs. SCE for 50 cycles in N_2-saturated 0.5 M H_2SO_4 aqueous solution to remove any surface contaminants. The electrochemically active surface area (ECSA) of the Pt electrocatalyst was calculated from the equation (ECSA = $Q/m \times C$) by measuring the charge collected in the hydrogen adsorption/desorption region after double-layer correction. Q is the charge in the hydrogen adsorption/desorption area, m is the loading amount of Pt metal, and C is the charge required for monolayer adsorption of hydrogen on a Pt surface ($C = 0.21$ mC·cm^{-2}).

For CO-stripping measurements, the catalyst surface was firstly saturated with CO by bubbling CO through a 0.5 M H_2SO_4 solution while holding the working electrode at 0 V for 15 min. The remaining CO was purged by flowing N_2 for 30 min before measurements were made.

2.4 Instruments

Transmission electron microscopy (TEM) images were obtained using a JEOL JEM-2100F transmission electron microscope operated at an accelerating voltage of 200 kV. Scanning electron microscopy (SEM) images were obtained using a JSM-2010 microscope at an accelerating voltage of 20 kV. X-ray diffraction (XRD) patterns of the samples were obtained with a Model D/max-rC X-ray diffractometer using a Cu Kα radiation source (λ = 1.5406 Å) and operating at 40 kV and 100 mA. X-ray photoelectron spectroscopy (XPS) measurements were performed with a Thermo VG Scientific ESCALAB 250 spectrometer with a monochromatic Al Kα X-ray source (1,486.6 eV photons). The binding energy was calibrated by means of the C1s peak energy of 284.6 eV. Ultraviolet and visible spectroscopy (UV–Vis) data were recorded on a Cary 50 spectrophotometer equipped with a 1.0 cm quartz cell.

3 Results and discussion

3.1 Characterization of samples

The crystal structure of the Pt-CNAs was initially characterized by XRD. The XRD pattern displays typical diffraction peaks that can be indexed as face-centered cubic (fcc) Pt (JCPDS no. 04-0802), indicating the generation of metallic Pt nanocrystals (Fig. 1(a)). The percentage of Pt^0 species in Pt-CNAs was calculated to be ca. 89.3% based on the XPS splitting peak-fitting curves (Fig. 1(b)), further confirming the complete reduction of the H_2PtCl_6 precursor. In particular, the XRD pattern of the Pt-CNAs shows a very strong (200) diffraction peak, indicating that the Pt-CNAs have abundant Pt {100} facets [26, 27]. According to Scherrer's formula, the average particle size of nanocrystals is estimated to be ca. 5.4 nm.

The morphology and structure of the Pt-CNAs were characterized by TEM and SEM. The TEM (Fig. 2(a)) and SEM (Fig. 2(b) and Fig. S1 in the Electronic Supplementary (ESM)) images clearly show that the products have well-defined cubic morphologies with porous cavities and rough surfaces. The average edge length of the Pt-CNAs was measured at ca. 120 nm. Based on the size analysis of the XRD and TEM, we speculate that each Pt-CNA is composed of many small nanocrystals ca. 5.4 nm in size. Interestingly, the selected-area electron diffraction (SAED) patterns of two random Pt-CNAs display a single set of sharp diffraction spots with 4-fold rotational symmetry (Fig. 2(c)), unambiguously demonstrating that the Pt-CNAs are single-crystalline with dominant Pt {100} facets. The high-resolution TEM (HRTEM) images obtained at different positions on an individual Pt-CNA in Fig. 2(d) show that the Pt-CNAs have dominant Pt {100} facets with 0.201 nm lattice spacing (Fig. 2(e)). This suggests that the preferred adsorption of the amine groups of arginine on the Pt-CNA surface during synthesis is responsible for the formation of dominant Pt {100} facets [28].

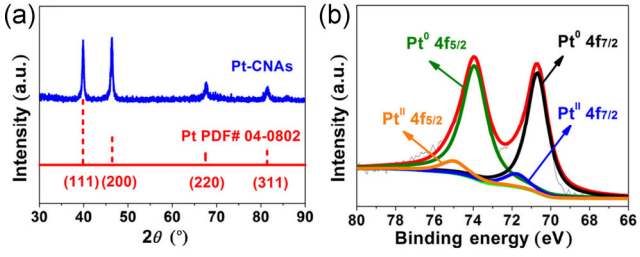

Figure 1 (a) XRD pattern and (b) Pt4f XPS spectrum of the Pt-CNAs.

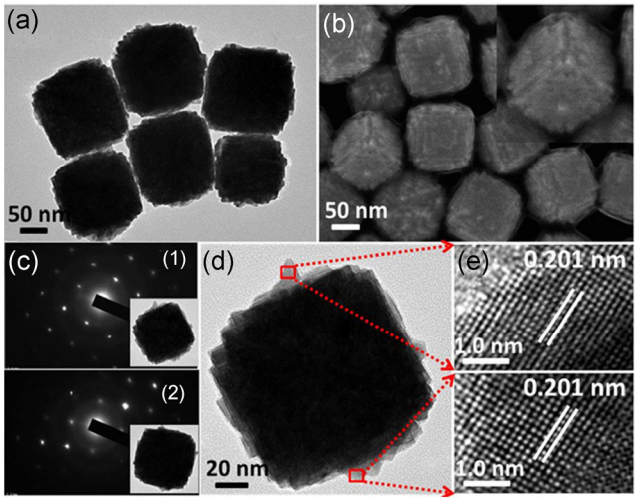

Figure 2 (a) TEM and (b) SEM images of the Pt-CNAs. Inset: magnified SEM image of an individual Pt-CNA. (c) SAED patterns of two different Pt-CNAs. (d) TEM image of an individual Pt-CNA. (e) HRTEM images recorded from the regions marked by the upper and lower squares in (d).

The shape evolution process of the Pt-CNAs was studied by obtaining TEM images of the Pt-CNAs at different times during the reaction (Fig. 3). At 0.5 h, we obtained sphere-like Pt nanocrystals with ca. 4 nm size (Fig. 3(a)). At 1 h, these small Pt nanocrystals started to grow into porous Pt nanoflowers with 70 nm size, wherein the primary Pt nanocrystals acted as building blocks (Fig. 3(b)). This evolution from small nanocrystals to nanoflowers clearly indicates that self-assembly occurs during the growth of Pt-CNAs. At 2 h, the porous Pt nanoflowers evolved into closely packed Pt nanoassemblies with sub-cubic morphology, accompanied by an increase in particle size to 90 nm (Fig. 3(c)). The decrease in pore size and the increase in particle size originate from the continuous reduction of the H_2PtCl_6 precursor. At 4 h, well-defined Pt-CNAs with ca. 120 nm size were generated (Fig. 3(d)). The time-dependent TEM images clearly indicate that the self-assembly of primary Pt nanocrystals and the continuous reduction of the H_2PtCl_6 precursor are responsible for the generation of the Pt-CNAs, as shown in Fig. 3(e).

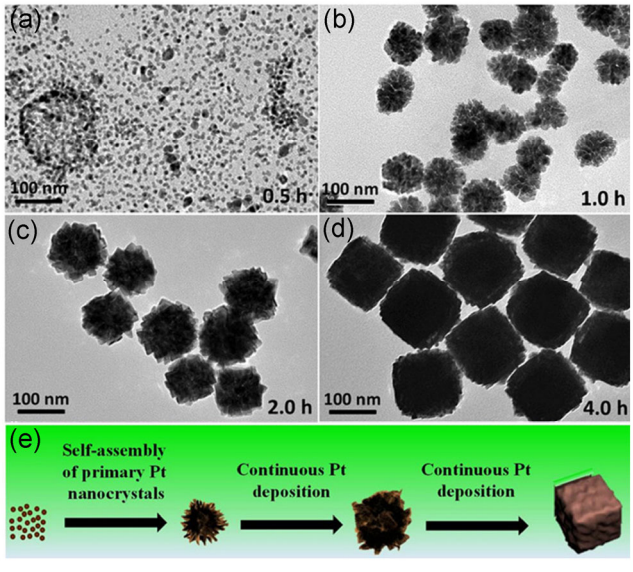

Figure 3 TEM images of the Pt intermediates collected at different growth stages: (a) 0.5, (b) 1, (c) 2, and (d) 4 h. (e) Proposed evolution mode of the Pt-CNAs.

A series of controlled experiments were performed to study the self-assembly-based growth mechanism. Firstly, we investigated the role of arginine by varying its amount while keeping other reaction conditions constant (Fig. 4). Only monodisperse Pt nanocrystals were obtained in the absence of arginine (Fig. 4(a)). When the amount of arginine was increased to 25 mg, small Pt nanocrystals started to self-assemble into chain-like nanostructures (Fig. 4(b)). The assembling feature of the Pt nanostructures, i.e., nanodendrites, became obvious when the amount of arginine was increased to 50 mg (Fig. 4(c)). On further increasing

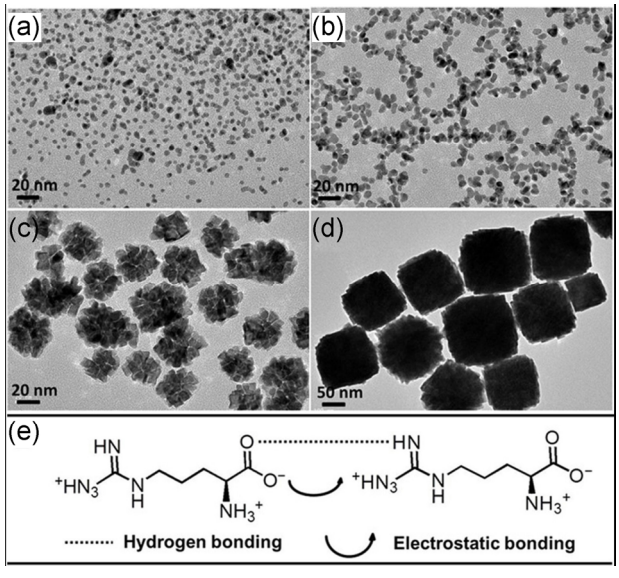

Figure 4 TEM images of the Pt nanostructures prepared using the standard procedure, except for the use of different amounts of arginine: (a) 0, (b) 25, (c) 50, and (d) 100 mg. (e) Proposed mechanism for the arginine-based self-assembly of detached Pt nanocrystals.

the amount of arginine to 75 mg (Fig. 2) and 100 mg (Fig. 4(d)), well-defined Pt-CNAs were the major products. These results indicate that the concentration of arginine plays a vital role in controlling the morphologies of Pt nanoassemblies, including nanochains, nanodendrites, and nanocubes.

In addition, it was also found that PVP molecules play an important part in the formation of the Pt-CNAs. We noted that Pt^{4+} ions also can be reduced by PVP in the absence of arginine (Fig. 4(a)), demonstrating that PVP effectively serves as a reducing agent under these conditions. In the absence of PVP, we obtained large chain-like nanostructures with obvious aggregation (Fig. S2 in the ESM), demonstrating that PVP not only acts as a reductant but also as a stabilizing agent. Thus, monodispersed Pt-CNAs can be obtained using the standard procedure, and the cubic and assembling features can be retained by adding excess PVP (600 mg) in the reaction system (Fig. S3 in the ESM).

According to the traditional viewpoint of dynamics, the fast nucleation and growth play an important role in the formation of the self-assembled nanostructures [29, 30]. Amino acid molecules, such as arginine, glycine, and lysine, can remarkably decrease the nucleation and growth rate of metal nanocrystals due to strong coordination interactions between the metal ions and amino acid molecules [15–20], which was confirmed by UV–Vis measurements (Fig. S4 in the ESM). Thus, the dynamics viewpoint cannot explain the coalescence of primary Pt nanocrystals during the formation of the Pt-CNAs. However, the slow reduction rate facilitates the formation of uniform products [31]. Indeed, the strong interaction between primary nanocrystals can also effectively facilitate their coalescence [29, 32]. Due to the strong amine-Pt interaction [28], the generated primary Pt nanocrystals can be concurrently functionalized by arginine during their generation, as confirmed by the N1s XPS spectrum (Fig. S5 in the ESM). Thus, the strong interactions between arginine molecules, including hydrogen-bonding and electrostatic interactions between amino and carboxyl groups, will effectively drive the self-assembly of arginine-functionalized Pt nanocrystals (Fig. 4(e)). Importantly, the arginine-mediated self-assembly process can also be extended to the synthesis of cube-like Pd nanoassemblies with Pd {100} facets (Fig. S6 in the ESM), demonstrating its universality. When lysine was used instead of arginine, sphere-like Pt nanoassemblies were obtained (Fig. S7 in the ESM), further confirming that the interaction between amino acid molecules facilitates the self-assembly of primary Pt nanocrystals.

3.2 Catalytic activity tests

The catalytic performance of the as-prepared Pt-CNAs for the MOR was investigated using an electrochemical measurement system. We benchmarked the electrocatalytic performance of the Pt-CNAs against that of commercial Pt black (Johnson Matthey). Figure 5(a) shows cyclic voltammetry (CV) curves of the Pt-CNAs and Pt black in N_2-saturated 0.5 M H_2SO_4 solutions at 50 $mV \cdot s^{-1}$. The ECSAs of the Pt-CNAs and Pt black, determined by measuring the charge of the hydrogen desorption region, were 10.8 and 17.5 $m^2 \cdot g^{-1}$, respectively [15, 16].

Figure 5(b) shows ESCA-normalized CVs for MOR on the Pt-CNAs and Pt black. Generally, the oxidation peak in the forward scan originates from methanol oxidation, while the backward scan oxidation peak is associated with the removable CO, which can act as a poisoning species [33]. In the forward scan, the peak current density of the MOR (2.62 $mA \cdot cm^{-2}$) at the Pt-CNAs is 2.73 times higher than that at the Pt black (0.96 $mA \cdot cm^{-2}$), showing improved specific activity. In Fig. 5(c), Pt-CNAs (3.50 $atom^{-1} \cdot s^{-1}$) exhibit a higher turnover frequency (TOF, defined here as the CH_3OH conversion per surface Pt atom per second) than Pt black (1.33 $atom^{-1} \cdot s^{-1}$), further confirming that the Pt-CNAs have higher specific activity than the commercial Pt black catalyst. It is noteworthy that the specific activity of the Pt-CNAs for the MOR is also higher than that of other Pt-based nanocrystals reported in the literature, such as Pt nanodendrites (0.9 $mA \cdot cm^{-2}$) [34], Pt nanoflowers (1.18 $mA \cdot cm^{-2}$) [35], mesoporous PtPdCu spheres (1.61 $mA \cdot cm^{-2}$) [36], Pt nanobars (1.70 $mA \cdot cm^{-2}$) [37], Pt–Au hollow nanourchins (2.25 $mA \cdot cm^{-2}$) [38], and Pt_3Ni networks (2.3 $mA \cdot cm^{-2}$) [39] (note: All measurements described in the literature were obtained in 0.5 M methanol). In addition, the trend of the mass activity of the abovementioned Pt-CNAs catalyst was also similar to that of the specific

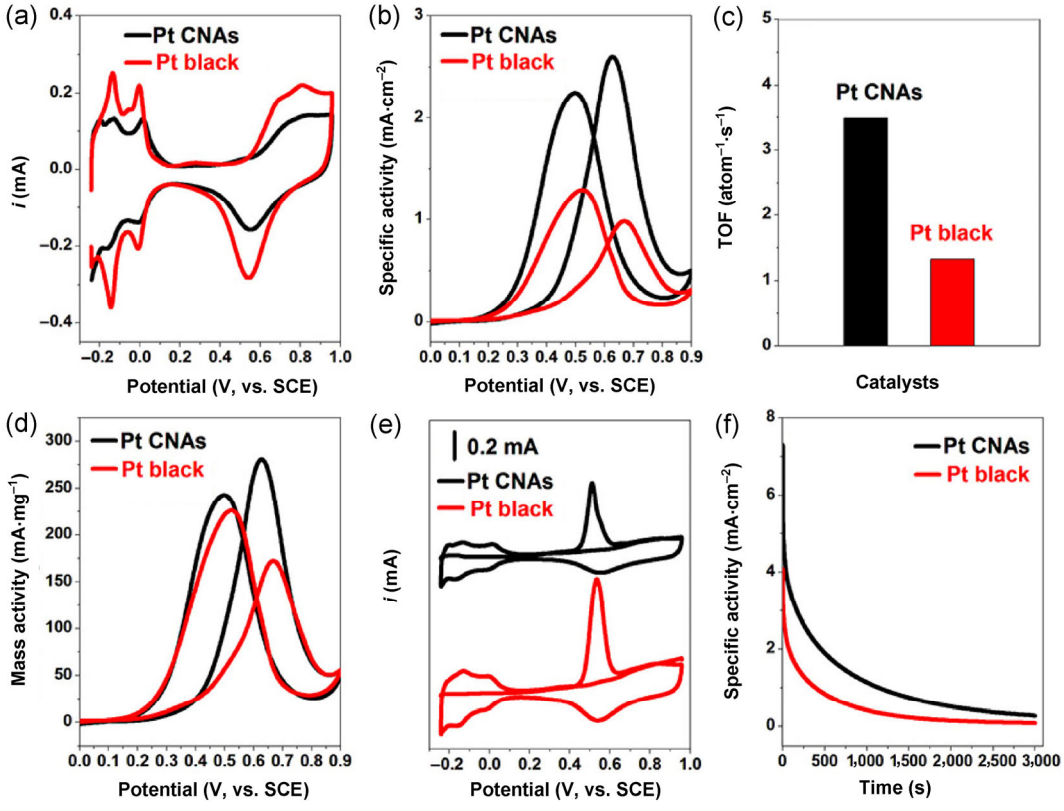

Figure 5 (a) CVs for the Pt-CNAs and Pt black in N_2-saturated 0.5 M H_2SO_4 solution at a scan rate of 50 mV·s^{-1}. (b) ESCA-normalized CVs for the Pt-CNAs and Pt black in N_2-saturated 0.5 M CH_3OH + 0.5 M H_2SO_4 solution at a scan rate of 50 mV·s^{-1}. (c) The TOFs of the Pt-CNAs and Pt black at 0.65 V. (d) Mass-normalized CVs for the Pt-CNAs and Pt black in N_2-saturated 0.5 M CH_3OH + 0.5 M H_2SO_4 solution at a scan rate of 50 mV·s^{-1}. (e) CO-stripping voltammograms for the Pt-CNAs and Pt black in N_2-saturated 0.5 M H_2SO_4 solution at a scan rate of 50 mV·s^{-1}. (f) Chronoamperometry curves for the Pt-CNAs and Pt black in N_2-saturated 0.5 M CH_3OH + 0.5 M H_2SO_4 solution for 3,000 s at 0.65 V.

activity. Figure 5(d) shows the Pt mass-normalized CVs for the MOR on the Pt-CNAs and Pt black. The peak current density of the MOR (278.64 mA·mg^{-1}) at the Pt-CNAs is 1.61 times higher than that at Pt black (173.45 mA·mg^{-1}), indicating that the Pt-CNAs hold promise as a potential practical electrocatalyst for the MOR. From XRD analysis, although the size of the Pt-CNAs (ca. 120 nm) is much greater than that of Pt black (ca. 8.5 nm), the size of the secondary building units of the Pt-CNAs (ca. 5.4 nm) is smaller than those of Pt black (ca. 8.5 nm) (Fig. S8 in the ESM); thus, the mass activity of the Pt-CNAs is also greater than that of Pt black. Furthermore, the Pt-CNAs can provide abundant porosity and a high internal reactive surface area due to their inherent structure, which facilitates mass diffusion of methanol molecules and electron transport during the MOR. Additionally, compared to the spherical Pt black catalyst with polycrystalline structure [37, 40, 41], the dominantly exposed {100} facets and abundant active sites at the edges and corners of the Pt-CNAs are likely also responsible for the enhanced MOR activity.

The ratio of the forward anodic peak current (I_f) to the backward anodic peak current (I_b), $R = I_f/I_b$, is an indicator of the CO tolerance of the electrocatalysts. As observed, the Pt-CNAs exhibit a higher R value (R = 1.16) than Pt black (R = 0.75), demonstrating the improved CO tolerance of the Pt-CNAs (Fig. 5(d)). To support this claim, we performed CO-stripping tests on our catalysts. Pt-CNAs show a negatively shifted peak potential of CO_{ad} oxidation compared to Pt black (Fig. 5(e)), suggesting that Pt-CNAs possess decreased affinity towards CO. Since the adsorption strength of CO species on Pt {100} facets is weaker than that on

Pt {111} facets, the dominantly exposed {100} facets of the Pt-CNAs may be responsible for the improved CO oxidation kinetics [42–44]. Besides efficiency and activity, the durability of an MOR electrocatalyst is also a key issue for the commercialization of fuel cells. Current–time (*i*–*t*) curves at 0.65 V potential show that current decay during the MOR at the Pt-CNAs is significantly slower than that at Pt black over the entire test range (Fig. 5(f)), indicating that the Pt-CNAs possess superior stability. We suspect that such assemblies can overcome the shortcomings of isolated small-size Pt nanocrystals related to dissolution, aggregation, and ripening during fuel cell operation [14, 45], which significantly improves the durability of the Pt-CNAs. Based on the above electrochemical investigations, we conclude that the Pt-CNAs may be suitable as highly active electrocatalysts for the MOR.

4 Conclusions

In summary, the strong interactions between amino acids molecules can effectively drive the self-assembly of primary metal nanocrystals to generate the nanoassemblies. Specifically we showed that cube-like Pt and Pd nanoassemblies could be easily obtained by arginine-mediated hydrothermal synthesis. By varying the concentration of arginine, we obtained Pt nanoassemblies with different morphologies. Benefiting from their unique structural features, the as-prepared Pt-CNAs exhibit excellent CO tolerance, improved electrocatalytic activity, and good stability for the MOR. We believe that they should be considered as promising electrocatalysts for electrochemical energy conversion applications.

Acknowledgements

This research was sponsored by National Natural Science Foundation of China (Nos. 21576139, 21503111, 21473111, 21376122, and 21273116), United Fund of National Natural Science Foundation (NSFC) and Yunnan Province (No. U1137602), Natural Science Foundation of Jiangsu Province (No. BK20131395), Natural Science Foundation of Shaanxi Province (No. 2015JM2043), Fundamental Research Funds for the Central Universities (No. GK201402016), China Scholarship Council (CSC, No. 201506860013), University Postgraduate Research and Innovation Project in Jiangsu Province (No. KYZZ15_0213), National and Local Joint Engineering Research Center of Biomedical Functional Material, and a project funded by the Priority Academic Program Development of Jiangsu Higher Education Institutions.

Electronic Supplementary Material: Supplementary material (experimental details, additional SEM, TEM images, XRD and XPS patterns and UV-vis results) is available in the online version of this article at http://dx.doi.org/10.1007/s12274-015-0899-3.

References

[1] Nie, Z. H.; Petukhova, A.; Kumacheva, E. Properties and emerging applications of self-assembled structures made from inorganic nanoparticles. *Nat. Nano.* **2010**, *5*, 15–25.

[2] Ying, J.; Yang, X.-Y.; Tian, G.; Janiak, C.; Su, B. L. Self-assembly: An option to nanoporous metal nanocrystals. *Nanoscale* **2014**, *6*, 13370–13382.

[3] Whitesides, G. M.; Grzybowski, B. Self-assembly at all scales. *Science* **2002**, *295*, 2418–2421.

[4] Wu, Z. N.; Li, Y. C.; Liu, J. L.; Lu, Z. Y.; Zhang, H.; Yang, B. Colloidal self-assembly of catalytic copper nanoclusters into ultrathin ribbons. *Angew. Chem.* **2014**, *126*, 12392–12396.

[5] Xia, B. Y.; Wu, H. B.; Li, N.; Yan, Y.; Lou, X. W. D.; Wang, X. One-pot synthesis of Pt–Co alloy nanowire assemblies with tunable composition and enhanced electrocatalytic properties. *Angew. Chem.* **2015**, *127*, 3868–3872.

[6] Ortiz, N.; Skrabalak, S. E. Manipulating local ligand environments for the controlled nucleation of metal nanoparticles and their assembly into nanodendrites. *Angew. Chem., Int. Ed.* **2012**, *51*, 11757–11761.

[7] Xia, B. Y.; Ng, W. T.; Wu, H. B.; Wang, X.; Lou, X. W. Self-supported interconnected Pt nanoassemblies as highly stable electrocatalysts for low-temperature fuel cells. *Angew. Chem., Int. Ed.* **2012**, *51*, 7213–7216.

[8] Nosheen, F.; Zhang, Z. C.; Xiang, G. L.; Xu, B.; Yang, Y.; Saleem, F.; Xu, X. B.; Zhang, J. C.; Wang, X. Three-dimensional hierarchical Pt-Cu superstructures. *Nano Res.* **2015**, *8*, 832–838.

[9] Hong, X.; Tan, C. L.; Liu, J. Q.; Yang, J.; Wu, X.-J.; Fan, Z. X.; Luo, Z. M.; Chen, J. Z.; Zhang, X.; Chen, B. et al. AuAg nanosheets assembled from ultrathin AuAg nanowires. *J. Am. Chem. Soc.* **2015**, *137*, 1444–1447.

[10] Gao, M. R.; Zhang, S. R.; Xu, Y. F.; Zheng, Y. R.; Jiang, J.; Yu, S. H. Self-assembled platinum nanochain networks

driven by induced magnetic dipoles. *Adv. Funct. Mater.* **2014**, *24*, 916–924.

[11] Hu, C. Y.; Lin, K. Q.; Wang, X. L.; Liu, S. J.; Yi, J.; Tian, Y.; Wu, B. H.; Chen, G. X.; Yang, H. Y.; Dai, Y. et al. Electrostatic self-assembling formation of Pd superlattice nanowires from surfactant-free ultrathin Pd nanosheets. *J. Am. Chem. Soc.* **2014**, *136*, 12856–12859.

[12] Henzie, J.; Grünwald, M.; Widmer-Cooper, A.; Geissler, P. L.; Yang, P. Self-assembly of uniform polyhedral silver nanocrystals into densest packings and exotic superlattices. *Nat. Mater.* **2011**, *11*, 131–137.

[13] Dong, A. G.; Chen, J.; Vora, P. M.; Kikkawa, J. M.; Murray, C. B. Binary nanocrystal superlattice membranes self-assembled at the liquid-air interface. *Nature* **2010**, *466*, 474–477.

[14] Sun, X. H.; Zhu, X.; Zhang, N.; Guo, J.; Guo, S. J.; Huang, X. Q. Controlling and self assembling of monodisperse platinum nanocubes as efficient methanol oxidation electrocatalysts. *Chem. Commun.* **2015**, *51*, 3529–3532.

[15] Zhang, Z. C.; Hui, J. F.; Liu, Z. C.; Zhang, X.; Zhuang, J.; Wang, X. Glycine-mediated syntheses of Pt concave nanocubes with high-index {*hk0*} facets and their enhanced electrocatalytic activities. *Langmuir* **2012**, *28*, 14845–14848.

[16] Xu, X. L.; Zhang, X.; Sun, H.; Yang, Y.; Dai, X. P.; Gao, J. S.; Li, X. Y.; Zhang, P. F.; Wang, H. H.; Yu, N. F. et al. Synthesis of Pt–Ni alloy nanocrystals with high-index facets and enhanced electrocatalytic properties. *Angew. Chem.* **2014**, *126*, 12730–12735.

[17] Qin, Y. C.; Zhang, X.; Dai, X. P.; Sun, H.; Yang, Y.; Shi, Q. X.; Gao, D. W.; Wang, H. Platinum-cobalt nanocrystals synthesized under different atmospheres for high catalytic performance in methanol electro-oxidation. *J. Mater. Chem. A* **2015**, *3*, 10671–10676.

[18] Fu, G.-T.; Wu, R.; Liu, C.; Lin, J.; Sun, D.-M.; Tang, Y.-W. Arginine-assisted synthesis of palladium nanochain networks and their enhanced electrocatalytic activity for borohydride oxidation. *RSC Adv.* **2015**, *5*, 18111–18115.

[19] Fu, G.-T.; Jiang, X.; Wu, R.; Wei, S.-H.; Sun, D.-M.; Tang, Y.-W.; Lu, T.-H.; Chen, Y. Arginine-assisted synthesis and catalytic properties of single-crystalline palladium tetrapods. *ACS Appl. Mater. Interfaces* **2014**, *6*, 22790–22795.

[20] Fu, G. T.; Liu, C.; Wu, R.; Chen, Y.; Zhu, X. S.; Sun, D. M.; Tang, Y. W.; Lu, T. H. L-lysine mediated synthesis of platinum nanocuboids and their electrocatalytic activity towards ammonia oxidation. *J. Mater. Chem. A* **2014**, *2*, 17883–17888.

[21] Shimoni, L.; Glusker, J. P. Hydrogen bonding motifs of protein side chains: Descriptions of binding of arginine and amide groups. *Protein Sci.* **1995**, *4*, 65–74.

[22] Pu, W. D.; Zhao, H. W.; Huang, C. Z.; Wu, L. P.; Xu, D. Visual detection of arginine based on the unique guanidino group-induced aggregation of gold nanoparticles. *Analyt. Chim. Acta* **2013**, *764*, 78–83.

[23] Fairlie, D. P.; Jackson, W. G.; Skelton, B. W.; Wen, H.; White, A. H.; Wickramasinghe, W. A.; Woon, T. C.; Taube, H. Models for arginine-metal binding. Synthesis of guanidine and urea ligands through amination and hydration of a cyanamide ligand bound to platinum(II), osmium(III), and cobalt(III). *Inorg. Chem.* **1997**, *36*, 1020–1028.

[24] Fu, G. T.; Liu, Z. Y.; Chen, Y.; Lin, J.; Tang, Y. W.; Lu, T. H. Synthesis and electrocatalytic activity of Au@Pd core-shell nanothorns for the oxygen reduction reaction. *Nano Res.* **2014**, *7*, 1205–1214.

[25] Crespo-Quesada, M.; Andanson, J. M.; Yarulin, A.; Lim, B.; Xia, Y. N.; Kiwi-Minsker, L. UV–ozone cleaning of supported poly(vinylpyrrolidone)-stabilized palladium nanocubes: Effect of stabilizer removal on morphology and catalytic behavior. *Langmuir* **2011**, *27*, 7909–7916.

[26] Wang, C.; Daimon, H.; Lee, Y.; Kim, J.; Sun, S. H. Synthesis of monodisperse Pt nanocubes and their enhanced catalysis for oxygen reduction. *J. Am. Chem. Soc.* **2007**, *129*, 6974–6975.

[27] Peng, Z. M.; Kisielowski, C.; Bell, A. T. Surfactant-free preparation of supported cubic platinum nanoparticles. *Chem. Commun.* **2012**, *48*, 1854–1856.

[28] Chen, M.; Kim, J.; Liu, J. P.; Fan, H. Y.; Sun, S. H. Synthesis of FePt nanocubes and their oriented self-assembly. *J. Am. Chem. Soc.* **2006**, *128*, 7132–7133.

[29] Ataee-Esfahani, H.; Skrabalak, S. E. Attachment-based growth: Building architecturally defined metal nanocolloids particle by particle. *RSC Adv.* **2015**, *5*, 47718–47727.

[30] Wang, F.; Li, C. H.; Sun, L. D.; Xu, C. H.; Wang, J. F.; Yu, J. C.; Yan, C. H. Porous single-crystalline palladium nanoparticles with high catalytic activities. *Angew. Chem., Int. Ed.* **2012**, *51*, 4872–4876.

[31] Xiong, Y. J.; Washio, I.; Chen, J. Y.; Cai, H. G.; Li, Z.-Y.; Xia, Y. N. Poly(vinyl pyrrolidone): A dual functional reductant and stabilizer for the facile synthesis of noble metal nanoplates in aqueous solutions. *Langmuir* **2006**, *22*, 8563–8570.

[32] Lv, W. Q.; He, W. D.; Wang, X. N.; Niu, Y. H.; Cao, H. Q.; Dickerson, J. H.; Wang, Z. Q. Understanding the oriented-attachment growth of nanocrystals from an energy point of view: A review. *Nanoscale* **2014**, *6*, 2531–2547.

[33] Mancharan, R.; Goodenough, J. B. Methanol oxidation in acid on ordered NiTi. *J. Mater. Chem.* **1992**, *2*, 875–887.

[34] Wang, J.; Zhang, X.-B.; Wang, Z.-L.; Wang, L.-M.; Xing, W.; Liu, X. One-step and rapid synthesis of "clean" and monodisperse dendritic Pt nanoparticles and their high performance toward methanol oxidation and p-nitrophenol reduction. *Nanoscale* **2012**, *4*, 1549–1552.

[35] Wang, M.; Wang, X. H.; Li, J. N.; Liu, L. T. *In situ* synthesis of 3D platinum nanoflowers on porous silicon for monolithic integrated micro direct methanol fuel cells. *J. Mater. Chem. A* **2013**, *1*, 8127–8133.

[36] Jiang, B.; Li, C. L.; Imura, M.; Tang, J.; Yamauchi, Y. Multimetallic mesoporous spheres through surfactant-directed synthesis. *Adv. Sci.* **2015**, *2*, 1246.

[37] Li, Y.; Bian, T.; Du, J. S.; Zhan, F. W.; Zhang, H.; Yang, D. R. Facile synthesis of high-quality Pt nanostructures with a controlled aspect ratio for methanol electro-oxidation. *CrystEngComm* **2014**, *16*, 8340–8343.

[38] You, H. J.; Zhang, F. L.; Liu, Z.; Fang, J. X. Free-standing Pt–Au hollow nanourchins with enhanced activity and stability for catalytic methanol oxidation. *ACS Catal.* **2014**, *4*, 2829–2835.

[39] Xu, Y.; Hou, S. X.; Liu, Y.; Zhang, Y.; Wang, H.; Zhang, B. Facile one-step room-temperature synthesis of Pt_3Ni nanoparticle networks with improved electro-catalytic properties. *Chem. Commun.* **2012**, *48*, 2665–2667.

[40] Lee, Y. W.; Han, S. B.; Kim, D. Y.; Park, K. W. Monodispersed platinum nanocubes for enhanced electrocatalytic properties in alcohol electrooxidation. *Chem. Commun.* **2011**, *47*, 6296–6298.

[41] Herrero, E.; Franaszczuk, K.; Wieckowski, A. Electrochemistry of methanol at low index crystal planes of platinum: An integrated voltammetric and chronoamperometric study. *J. Phys. Chem.* **1994**, *98*, 5074–5083.

[42] Urchaga, P.; Baranton, S.; Coutanceau, C.; Jerkiewicz, G. Electro-oxidation of CO_{chem} on Pt nanosurfaces: Solution of the peak multiplicity puzzle. *Langmuir* **2012**, *28*, 3658–3663.

[43] Coutanceau, C.; Urchaga, P.; Baranton, S. Diffusion of adsorbed CO on platinum (100) and (111) oriented nanosurfaces. *Electrochem. Commun.* **2012**, *22*, 109–112.

[44] Coutanceau, C.; Lamy, C.; Urchaga, P.; Baranton, S. Platinum activity for CO electrooxidation: From single crystal surfaces to nanosurfaces and real fuel cell nanoparticles. *Electrocatalysis* **2012**, *3*, 304–312.

[45] Niu, Z. Q.; Wang, D. S.; Yu, R.; Peng, Q.; Li, Y. D. Highly branched Pt-Ni nanocrystals enclosed by stepped surface for methanol oxidation. *Chem. Sci.* **2012**, *3*, 1925–1929.